The Astrophysical Journal, 761:76 (11pp), 2012 December 10 doi:10.1088/0004-637X/761/1/76

PROPER MOTIONS AND ORIGINS OF SGR 1806−20 AND SGR 1900 + 14

Shriharsh P. Tendulkar[1], P. Brian Cameron[2], and Shrinivas R. Kulkarni[1]
[1] California Institute of Technology, 1200 E California Blvd, MC 249-17, Pasadena, CA 91125, USA; spt@astro.caltech.edu
[2] The Aerospace Corporation, 15049 Conference Center Drive, Chantilly, VA 20151-3824, USA
Received 2012 August 16; accepted 2012 October 27; published 2012 November 27

ABSTRACT

We present results from high-resolution infrared observations of magnetars SGR 1806−20 and SGR 1900+14 over 5 years using laser-supported adaptive optics at the 10 m Keck Observatory. Our measurements of the proper motions of these magnetars provide robust links between magnetars and their progenitors and provide age estimates for magnetars. At the measured distances of their putative associations, we measure the linear transverse velocity of SGR 1806−20 to be $350 \pm 100\,\mathrm{km\,s^{-1}}$ and of SGR 1900+14 to be $130 \pm 30\,\mathrm{km\,s^{-1}}$. The transverse velocity vectors for both magnetars point away from the clusters of massive stars, solidifying their proposed associations. Assuming that the magnetars were born in the clusters, we can estimate the braking index to be ∼1.8 for SGR 1806−20 and ∼1.2 for SGR 1900+14. This is significantly lower than the canonical value of $n = 3$ predicted by the magnetic dipole spin-down suggesting an alternative source of dissipation such as twisted magnetospheres or particle winds.

Key words: proper motions – stars: individual (SGR 1806−20, SGR 1900+14) – stars: magnetars – stars: neutron

Online-only material: color figures

1. INTRODUCTION

Magnetars were proposed (Thompson & Duncan 1995, 1996) as a unified model to explain the phenomena of soft gamma repeaters (SGRs) and anomalous X-ray pulsars (AXPs). Magnetars, unlike canonical radio pulsars, would have a very high magnetic field strength B ($\sim 10^{14}$ G) such that their internal energy was dominated by their magnetic energy rather than their rotational energy. The SGR flares were explained as resulting from violent magnetic reconnections and crustal quakes and the quiescent X-ray emission of AXPs (which is much larger than their spin-down luminosity) was attributed to the decay of intense magnetic fields. The discovery of large period derivatives ($\dot{P} \sim 10^{-10}\,\mathrm{s\,s^{-1}}$; Kouveliotou et al. 1998) confirmed the basic expectation of the magnetar model. For recent reviews of observational and theoretical progress in the field, we refer the readers to Mereghetti (2008) and Hurley (2011).

Despite the successes of the magnetar model, we have little understanding of why only some neutron stars are born as magnetars. Originally, Thompson & Duncan (1993) invoked a rapidly spinning (∼1–3 ms) proto-neutron star as essential for strong amplification of a seed magnetic field. The rapidly spinning neutron stars would result in a supernova more energetic than a canonical core-collapse supernova.

The observational support for the formation mechanism of magnetars appears to be lacking. Vink & Kuiper (2006) showed that the three supernova remnants (SNRs) to which three magnetars are best paired (Kes 73, CTB 109, and N49) are completely consistent with the standard supernova explosion energies.

The offset between SGR 0525−66 (previously known as "1979 March 5") and its surrounding SNR N49 and the notion that some halo SGRs might explain a fraction of gamma-ray bursts (GRBs) led to the expectation of SGRs having high space motion (see Rothschild & Lingenfelter 1996). This spawned a number of efforts to measure the space motions of magnetars.

Here, we present astrometric observations of two of the youngest magnetars: SGR 1806−20 and SGR 1900+14. The resulting measurements of proper motion allow us to trace back these two objects to their potential birth sites and additionally measure the space motions as well. The paper is organized as follows. In Section 2, we summarize our knowledge of these two magnetars. In Section 3, we describe our observations, data reduction methodology, and analysis techniques for point-spread function (PSF) fitting, relative astrometry, and photometry. We present the results in Section 4 and in Section 5 we discuss the significance of our proper motion measurements.

2. TARGETS

Table 1 summarizes the essential characteristics of both our targets: SGR 1806−20 and SGR 1900+14. We discuss each target in further detail in the following sections.

2.1. SGR 1806−20

SGR 1806−20 (previously known as GB790107) was identified as a repeating GRB with a soft spectrum by Laros et al. (1986). SGR 1806−20 is best known for its giant burst of 2004 December 27 (Hurley et al. 2005; Palmer et al. 2005), which was one of the brightest cosmic flares ever detected. The burst was followed by a long-lived radio afterglow (Cameron et al. 2005; Gaensler et al. 2005; Spreeuw et al. 2010), which allowed the precise localization of the source.

2.1.1. Association with Star Cluster

SGR 1806−20 lies in a radio nebula G10.0−0.3 (Kulkarni et al. 1995), which is a part of the W31 HII complex. It was earlier suggested that the massive star LBV 1806−20 and its surrounding radio nebula were associated with SGR 1806−20 (van Kerkwijk et al. 1995) but precise *Chandra* localization (Kaplan et al. 2002) proved that SGR 1806−20 was 14″ away from the center of G10.0−0.3 and 12″ away from LBV 1806−20. A cluster of massive stars, coincident with a mid-IR nebulosity, was discovered by Fuchs et al. (1999) about 7″ to the north of the magnetar.

Table 2 lists all the distance measurements reported to date. We place a higher premium for distance estimates related to the X-ray counterpart of SGR 1806−20 or the associated cluster of massive stars over the estimates to LBV 1806−20, since it is unclear whether LBV 1806−20 is physically near the magnetar.

Table 1
Characteristics of SGR 1806−20 and SGR 1900+14

	SGR 1806−20	SGR 1900+14
Period P (s)	7.6022(7)	5.19987(7)
$\dot{P}$ (10^{-11} s s^{-1})[a]	49	17
$P/\dot{P}$ (kyr)	0.32	1.8
$B_{\rm Surf}$ (10^{14} G)	24	7.0
R.A. (J2000)	$18^{\rm h}08^{\rm m}39\overset{\rm s}{.}337$	$19^{\rm h}07^{\rm m}14\overset{\rm s}{.}31$
Decl. (J2000)	$20^\circ24'39\overset{''}{.}85$	$9^\circ19'19\overset{''}{.}74$

Notes. Refer to http://www.physics.mcgill.ca/~pulsar/magnetar/main.html. Positions are from *Chandra* X-ray observations.
[a] Average period derivative calculated from X-ray period measurements from literature. See Section 5.2.

In Table 2, measurements 1–4 are distances to SGR 1806−20 or the cluster of massive stars and measurements 5 and 6 are distances to LBV 1806−20. We adopt a nominal distance of 9 ± 2 kpc, which is consistent with all the measurements.

2.1.2. IR Counterpart

Figure 1 shows a 2 × 2 arcsec cutout near SGR 1806−20 from our laser guide star adaptive optics (LGS-AO) supported observations in the K_s band using the Near-Infrared Camera 2 (NIRC2) instrument (See Section 3 for details). Star A was suggested as the NIR counterpart for SGR 1806−20 by Kosugi et al. (2005) and independently by Israel et al. (2005) based on NIR variability over the 2004 active period. Using the NAOS-CONICA instrument on the 8.1 m Very Large Telescope (VLT), Israel et al. (2005) monitored SGR 1806−20 on 11 epochs between 2004 March and October. They measured a factor of two increase in the flux of the star A with a $>9\sigma$ confidence. The IR flux increase corresponded well with X-ray flux that also increased by a factor of two in the 2–10 keV and 20–100 keV bands (*XMM-Newton, INTEGRAL*; Mereghetti et al. 2005b, 2005a). Our photometric measurements show a factor of three variability in the brightness of the same object (Section 4.1). The identification of the IR counterpart of SGR 1806−20 appears to be secure.

2.2. SGR 1900+14

The first bursts from SGR 1900+14 (originally known as B1900+14) were identified by Mazets et al. (1979). A very bright flare was detected on August 27 1998 with a γ-ray peak followed by a 300 s long tail (Hurley et al. 1999; Kouveliotou et al. 1999). Following the burst, a fading radio (Frail et al. 1999)

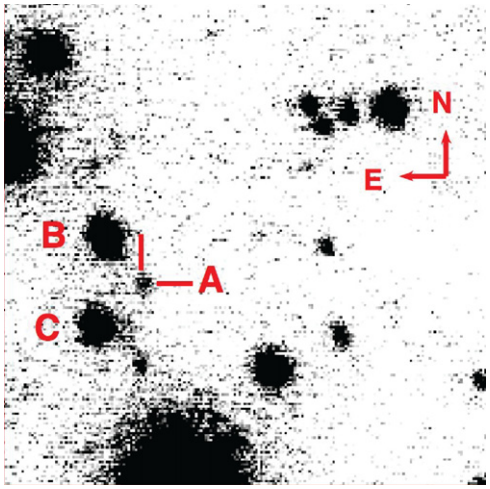

Figure 1. 2 × 2 arcsec cutout near SGR 1806−20 from a K_s-band LGS-AO supported observation from the NIRC2 camera. The IR counterpart, as identified by Kosugi et al. (2005) and Israel et al. (2005), is marked with cross hairs and labeled A as per Israel et al. (2005) as are stars B and C.
(A color version of this figure is available in the online journal.)

and an X-ray source (Hurley et al. 1999) were discovered. These observations led to a precise localization to within $0\overset{''}{.}15$.

2.2.1. Association with Star Cluster

SGR 1900+14 is located near two objects from which it could have originated. A cluster of massive stars (Vrba et al. 2000), hidden behind two bright M5 super-giants, lies 12″ to the east of SGR 1900+14 and a 10^4 yr old, 12′ diameter SNR G042.8+00.6 lies 17′ to the southeast (Mazets et al. 1979; Kouveliotou et al. 1993; Vasisht et al. 1994). If SGR 1900+14 was associated with the cluster of massive stars then it implies a young age and a space velocity close to the canonical value for pulsars. However, if it is associated with the SNR then it would have a very high proper motion. An upper limit to the proper motion (based on *Chandra X-ray observatory* imaging observations) of $\leqslant$100 mas yr^{-1} is nominally inconsistent with the association of SGR 1900+14 with the SNR (Kaplan et al. 2009; de Luca et al. 2009).

Wachter et al. (2008) reported the discovery of an infrared elliptical ring or shell surrounding SGR 1900+14, which was interpreted as a dust-free cavity created by the giant flare of 1998 August. The authors concluded that SGR 1900+14 is unambiguously associated with the aforementioned star cluster.

With AO assisted Keck/NIRC2 imaging and Keck/NIRSPEC spectroscopy of the cluster near SGR 1900, Davies et al. (2009)

Table 2
Distance to SGR 1806−20 Measured by Various Authors

	Reference	Distance (kpc)	Comments
1	Cameron et al. (2005)	6.5–9.8	H I absorption from 2004 Dec flare
2	McClure-Griffiths & Gaensler (2005)	>6.5	H I absorption from 2004 Dec flare
3	Svirski et al. (2011)	9.4 − 18.6	X-ray scattering echos
4	Bibby et al. (2008)	$8.7^{+1.8}_{-1.5}$	Spectral classification, IR photometry and cluster isochrones
5	Figer et al. (2004)	11.8 ± 0.5	Radial velocity (RV) of LBV 1806
6	Eikenberry et al. (2004)	$15^{+1.8}_{-1.3}$	RV of LBV 1806 and surrounding nebula and Galactic rotation curve
		Strictly >9.5	Luminosity of cluster stars
		Strictly >5.7	Ammonia absorption to LBV 1806

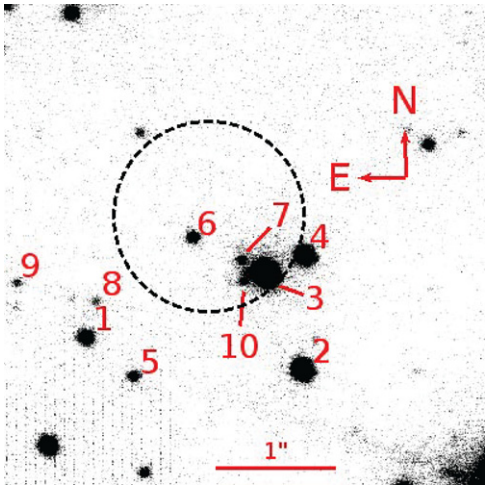

Figure 2. 4 × 4 arcsec cutout near SGR 1900+14 from a K_s-band LGS-AO supported observation from the NIRC2 camera. Stars are labeled as per Testa et al. (2008). The black circle is centered on the radio position of SGR 1900+14 from Frail et al. (1999) and encircles the 0.″8 radius, 99% confidence position error from Testa et al. (2008). We use the Testa et al. (2008) positions for absolute astrometry. Star 7 is the proposed counterpart of SGR 1900+14 based on its variability.

(A color version of this figure is available in the online journal.)

estimated the progenitor mass to be $17 \pm 2\ M_{\odot}$, which is much lower than the progenitor masses estimated for other magnetars ($\sim$40 to 50 $M_{\odot}$).

2.2.2. Distance

Vrba et al. (1996) showed that the bright IR sources noted by Hartmann et al. (1996) at the *ROSAT* localization of SGR 1900+14 were M5 super-giant stars at a distance of 12–15 kpc with an extinction of $A_V \approx 19.2$ mag. Davies et al. (2009) measured a radial velocity of $-15.5 \pm 4\,\mathrm{km\,s^{-1}}$ for the cluster of stars implying a distance of 12.5 ± 1.7 kpc using the measured model of Galactic rotation. We adopt the measurement of Davies et al. (2009) for the distance to SGR 1900+14.

2.2.3. IR Counterpart

Figure 2 shows a 4 × 4 arcsec K_s-band image from our LGS-AO observations with the NIRC2 camera around the X-ray position of SGR 1900+14. The stars are labeled as per Testa et al. (2008). They obtained two K_S-band AO observations of the same field around SGR 1900+14 with VLT NACO instrument in 2006 March and July. Star 7 was the only source inside the radio-position error circle (dashed circle in Figure 2) that showed a photometric variability. They detected a 3σ increase in the flux of star 7 and proposed it as the IR counterpart of SGR 1900+14. We accept the counterpart proposed by Testa et al. (2008).

In an attempt to gather additional evidence for the identification of the IR counterpart, we have measured K_p-band photometric variability and $H - K_p$ color for the stars in the field. These measurements are reported in Section 4.2. However, during this period, the X-ray counterpart did not show significant variability. Hence the absence of NIR variation of the proposed counterpart does not provide any new insights.

We report (in Section 4) that the proper motion of star 6 lies along the Galactic rotation curve, whereas the proper motion of star 7 is significantly different from those of galactic stars. This evidence strengthens the identification of star 7 as the IR counterpart of SGR 1900+14.

Table 3
Summary of Observations of SGR 1806−20

Date and MJD (UTC MJD)	Filt	Cam	Exp (s)
2005 March 4 53433.641	K_p	N	1440 ✓
2005 April 30 53490.511	K_p	N	750
2005 August 10 53592.366	K_p	W	600
2005 August 11 53593.344	K_p	W	840
2005 September 26 53639.258	K_p	N	600 ✓
2006 July 03 53919.403	K_p	N	2820
2006 August 17 53964.304	K_p	N	1800 ✓
2007 May 22 54242.487	K_p	N	1020
2007 June 11 54262.403	K_p	N	2040
2007 July 16 54297.345	K_p	N	3000
2007 August 06 54318.329	K_p	N	2640 ✓
2008 May 21 54607.468	K_p	N	2460
2008 June 29 54646.407	K_p	N	3360
2008 July 26 54673.342	K_p	N	3180 ✓
2010 June 18 55365.442	K_p	W	80

Note. A ✓ in Column 4 marks the images used for astrometric measurements.

Table 4
Summary of Observations of SGR 1900+14

Date and Time (UTC)	Filt	Cam	Exp (s)
2005 April 30 53490.558	K_p	N	1300 ✓
2005 August 09 53591.434	K_p	W	2400
2005 August 10 53592.400	K_p	W	300
2005 September 26 53639.349	K_p	W	720
2006 July 03 53919.472	K_p	N	1980
2006 July 04 53920.511	K_p	N	1920
2006 August 17 53964.439	K_p	N	1140 ✓
2006October 13 54021.242	K_p	N	2220
2007 May 22 54242.550	K_p	N	1500 ✓
2007 June 11 54262.553	K_p	N	1260 ✓
2007 June 11 54262.582	H	N	660
2007 August 06 54318.455	K_p	N	1800 ✓
2007 November 03 54407.229	K_p	N	1260 ✓
2008 May 21 54607.564	K_p	N	1260
2008 June 29 54646.471	K_p	N	3660
2008 July 26 54673.405	K_p	N	2280 ✓
2008 October 22 54761.227	K_p	N	1680 ✓
2009 April 06 54927.599	K_p	N	1620
2009 July 17 55029.340	K_p	N	2100 ✓
2009 August 04 55047.346	K_p	N	2100
2009 September 29 55103.226	K_p	N	2340
2010 June 18 55365.470	K_p	N	2340 ✓

Note. A ✓ in Column 4 marks the images used for astrometric measurements.

3. OBSERVATIONS AND ANALYSIS

3.1. Observations

Starting in 2005 to the present time, we undertook a program for astrometric monitoring of magnetars with the 10 m Keck 2 telescope using the LGS-AO (Wizinowich et al. 2006; van Dam et al. 2006) and the NIRC2. The log of our observations can be found in Tables 3 and 4.

3.1.1. NIRC2

The NIRC2 instrument has two modes: wide (W) and narrow (N) with a field of view (FoV) of ≈10 × 10 arcsec and ≈40 × 40 arcsec, respectively. The corresponding pixel scales are 9.942 mas pixel^{-1} and 39.768 mas pixel^{-1}. The wide

field images were obtained to aid transferring the photometry and astrometry from the low resolution Two Micron All Sky Survey (2MASS) images to the small FoV narrow camera NIRC2 images. The narrow field images were used for the astrometric measurements. Based on weather and faintness of each magnetar, multiple short (∼20 s) exposures were chosen to avoid saturating the detector. The typical full width at half-maximum (FWHM) achieved in these observations was ≈70 mas ≈7 pixel.

Each of the NIRC2 narrow camera images was inspected for quality control. Images in which the AO correction was poor were rejected. The shallow images with acceptable AO correction were rejected for astrometry due to the non-detection of the magnetar and/or lack of sufficient reference stars but were used to photometric calculate upper limits on the brightness. The images used in the final proper motion measurement are denoted by a ✓ in Column 4 of Tables 3 and 4.

3.2. Data Analysis

The images from the NIRC2 camera were reduced using the FITS analysis package `pyraf` in a standard manner by subtracting corresponding dark frames and flat-fielded using appropriate dome flats. A sky fringe frame was made by combining dithered images of multiple targets with the bright stars masked. We used `SExtractor` (Bertin & Arnouts 1996) for the preliminary detection and masking of stars. The fringe frame was subtracted after being scaled to the appropriate sky background level. Before co-adding the frames, each frame was corrected for optical distortion using a distortion solution measured for NIRC2.[3]

3.2.1. PSF Fitting

We used the `IDL` package `StarFinder` (Diolaiti et al. 2000) to perform PSF estimation, fitting, and subtraction. This code iteratively estimates a normalized PSF shape from user-selected stars, while subtracting faint neighboring stars to minimize the contamination of the PSF estimate. `StarFinder` fits a constant PSF shape over the entire FoV. This assumption appears to work well for the NIRC2 narrow camera FoV. The uniformity of the PSF over the FoV also mitigates the errors from centroiding variable PSFs.

AO PSFs differ from PSFs obtained from atmospheric seeing limited observations in two aspects. First, because the AO correction decorrelates as a function of distance from the AO reference source (i.e., sodium laser beacon), the PSF varies radially across the FoV. Second, since AO correction cannot correct all of the wavefront errors caused by atmospheric turbulence, even on-axis, AO PSFs have a distinctive shape with a sharp diffraction-limited (FWHM $\sim \lambda/D_{\rm tel}$) core and a wide (FWHM ∼ atmospheric seeing) shallow halo around it. For the Keck AO system, these components are 44 mas and ∼1 arcsec, respectively. The order of magnitude difference in size and brightness of the two components makes it challenging to accurately measure and subtract the PSF in the image. We describe how both these challenges are handled in the next paragraph.

To further reduce the effect of PSF variations, relative photometry and astrometry measurements were down weighted farther away from the object under consideration. The details of the relative weighting are described in Section 3.2.2. The PSF model size was chosen to be 200 pixels (1.95 arcsec) wide to encompass both the core and the halo of the PSF. The few brightest stars in each of the fields were used for estimating the halo contribution.

3.2.2. Relative Astrometry

Cameron et al. (2009) demonstrated a framework for high precision astrometry (<100 μarcsec) through an optimal estimation technique that availed the correlations in stellar position jitter. We use the same methodology with modifications for including the proper motions of the stars over multiple epochs and an appropriate weighting scheme.

The dominant source of astrometric error in the single epoch, short exposure images of Cameron et al. (2009) was tip-tilt anisoplanatism. For our co-added long exposure images, the tip-tilt anisoplanatism is averaged out. We constructed the covariance matrix theoretically using geometry of the field and a typical turbulence profile from Mauna Kea. The residual distortion of the NIRC2 distortion solution has a root-mean-square value of 1 mas. However, the distortion residuals have higher values toward the edges.[3] To reduce the effect of residual distortion, especially in images with significant dithering, a separation-weighted measurement scheme (the θ term used below) was used to down weight stars far from the target.

To account for the proper motions of all the stars in the field, it was necessary to include the proper motion estimates in the framework and simultaneously estimate a least-squares fit for grid positions and proper motions. Given $N+1$ stars detected in the field, the measurement of the offset between the target star and each of the remaining stars results in a set of vectors at each of the E epochs.

The differential offsets between star 0 and the grid of N reference stars at epoch k are written as a single column vector,

$$\mathbf{d}_{0k} = [x_{01}, \ldots, x_{0N}, y_{01}, \ldots, y_{0N}]_k^T.$$

Here, $x_{ij} = x_j - x_i$ is the distance between the x-coordinate of the jth reference star and the x-coordinate of the ith target star, and likewise for y. The goal of differential astrometry is to use $\mathbf{d}$ to determine the position of the target star with respect to the reference grid of stars at each epoch.

We use a linear combination of the elements of $\mathbf{d}$ with weights $\mathbf{W_i}$ to obtain the relative position of target star i at epoch k,

$$\mathbf{p}_{ik} = \mathbf{W}_i \mathbf{d}_{ik},$$

where, for example, the weight matrix for star 0, $\mathbf{W}_0$, is

$$\mathbf{W}_0 = \begin{bmatrix} w_{xx,01} & \ldots & w_{xx,0N} & w_{xy,01} & \ldots & w_{xy,0N} \\ w_{yx,01} & \ldots & w_{yx,0N} & w_{yy,01} & \ldots & w_{yy,0N} \end{bmatrix}.$$

We calculated weights as follows: $w_{xx,ij}^{-1} = w_{yy,ij}^{-1} = \sigma_{ij}^2$. Here $\sigma_{ij}^2 = \sigma_m^2 + \sigma_{TJ}^2 \theta_{ij}^2$, where σ_{TJ}^2 is the geometric mean of the parallel and perpendicular components of the tip-tilt jitter as defined in Equation (1) of Cameron et al. (2009); and θ_{ij} is the angular offset between the star i and the star j. We have used the notation $w_{xy,0j}$ to denote the weighting of the offset from the target star ($i = 0$) to star indexed j in the y-direction, which is used to determine the x component of the target's position, $\mathbf{p}$.

[3] See http://www2.keck.hawaii.edu/inst/nirc2/forReDoc/post_observing/dewarp/.

We assume a simple linear model for the stellar motion where $x = z_x + v_x t$. The differential offsets are thus a column vector,

$$\mathbf{d}_0 = \begin{bmatrix} z_{x,1} + v_{x,1}t - (z_{x,0} + v_{x,0}t) \\ \vdots \\ z_{x,N} + v_{x,N}t - (z_{x,0} + v_{x,0}t) \\ z_{y,1} + v_{y,1}t - (z_{y,0} + v_{y,0}t) \\ \vdots \\ z_{y,N} + v_{y,N}t - (z_{y,0} + v_{y,0}t) \end{bmatrix}$$

and the unknown quantities are

$$\mathbf{b} = [z_{x,0}, \quad \ldots \quad , z_{x,N}, v_{x,0}, \ldots, v_{x,N}, \tag{1}$$

$$\ldots, z_{y,0}, \quad \ldots \quad , z_{y,N}, v_{y,0}, \ldots, v_{y,N}]^T. \tag{2}$$

We solve for the variables **b** from the vector **d** given weights **W** in the least-squares sense. For a given target, we use the same weights for all epochs. The overall x and y shifts of each image (i.e., the registration of the image) are fit as free parameters in this method.

NIRC2 is mounted at the Nasmyth focus of the Keck II telescope. A field rotator allows the observer to set the position angle of the instrument. Our default position angle was 0 deg (north is up and east is to the left on the detector). However, there are small errors in the setting of the field rotator as well as tracking errors.

To measure this, we chose the images obtained on 2007 May 22 as the reference image for both the targets. The reference images were chosen on the basis of good AO correction and image depth. We computed the rotation angle and the plate scale of the image at each epoch with respect to the reference image. We find that the rotation angle is within 0.5 deg and the image scaling is within 0.1% relative to those of the reference image. The stellar position grids were corrected for the measured rotation and plate-scale changes before measuring their proper motions.

To understand the systematic effects caused by our choice of grid stars, we re-analyzed the centroiding data after randomly eliminating a selected number of stars from the reference grid. We compared the results to those obtained from our entire grid of stars. For example, by eliminating one randomly chosen star out of the 50 stars in the SGR 1900+14 field, the proper motions of all other stars change by $\Delta(\mu_\alpha, \mu_\delta) = (7.6 \pm 15.4, 17.1 \pm 13.7) \times 10^{-3}$ mas yr^{-1}. This is much smaller than our statistical errors of $\sim$1 mas yr^{-1}. Hence we conclude that the choice of our reference grid is robust and does not add significant errors to our measurements.

3.2.3. Galactic Rotation

Since our relative astrometry framework calculates the proper motion of each object with respect to a grid of neighboring stars (i.e., with respect to the average motion of all other stars), it implicitly assumes that the net velocity of the field is zero. However, this is not true since the rotation of the Galaxy and the peculiar velocity of the Sun with respect to the local standard of rest cause significant motions at the precision we seek. Our framework cannot measure the net velocity of the field without prior knowledge of the absolute motion of a few stars or equivalently, the absolute non-motion of an extra-galactic object in the field.

Table 5
Proper Motions Calculated from the Galactic Rotation Model as Described in Section 3.2.3

Object ID	Distance (kpc)	(l, b) (deg)	$\boldsymbol{\mu}_{\rm Field}$ $[\mu_\alpha, \mu_\delta]$ (mas yr^{-1})	$\boldsymbol{\mu}_{\rm Gal}$ $[\mu_\alpha, \mu_\delta]$ (mas yr^{-1})
SGR 1806−20	9 ± 2	(10.0, −0.2)	[3.0, 4.8]	$[4.2 \pm 0.9, 7.0 \pm 1.8]$
SGR 1900+14	12.5 ± 1.7	(43.0, +0.8)	[2.7, 4.6]	$[2.7 \pm 0.2, 4.8 \pm 0.4]$

To correct for this effect, we need to calculate the mean galactic proper motion of all the stars in the field along the line of sight given by Galactic longitude and latitude (l, b). We modeled the differential rotation of the Galaxy and the local velocity of the Sun and calculated the effective proper motion of an object at a given position (r, l, b) in the Milky Way, where r is the distance away from the Sun. We made a model assuming the local velocity of the Sun to be $(U, V, W) = (10.0, 5.2, 7.2)$ km s^{-1} (Dehnen & Binney 1998) and that the Galaxy is rotating with a constant circular speed outside of $R_1 = 2$ kpc of 220 km s^{-1}, decreasing linearly inside of that R_1 (Binney & Tremaine 2008). We set the distance from the Sun to the center of the Galaxy to $R_0 = 8.0$ kpc (Eisenhauer et al. 2003). From the rotation curve, we calculate the Galactic proper motion $\boldsymbol{\mu}_{\rm Gal} = [\mu_\alpha, \mu_\delta]_{\rm Gal}$ of objects at various distances (1 kpc $\leqslant r \leqslant$ 20 kpc) in the direction (l, b) of the magnetar that are moving with the Galactic flow.

We estimate the number density of stars in the Milky Way using the model calculated by Jurić et al. (2008) using Sloan Digital Sky Survey (SDSS) data. They fit a thin disk, a thick disk, and a halo to the SDSS data set and calculate the number density function based on their fit. Along the line of sight, the number of stars in our field at a distance r from the Sun is proportional to $r^2\rho(R, Z)$, where $\rho(R, Z)$ is the number density of stars at the cylindrical coordinates $(R(r, l, b), Z(r, l, b))$ in the Milky Way.

For a given field, we calculate the velocity of the field $\boldsymbol{\mu}_{\rm Field} = [\mu_\alpha, \mu_\delta]_{\rm Field}$ as the integral of the proper motion weighted with the number density as described above. This gives

$$\boldsymbol{\mu}_{\rm Field} = \frac{\int_{r_{\rm min}}^{r_{\rm max}} r^2 \rho(R(r,l,b), Z(r,l,b)) \times [\mu_{\alpha,\delta}(r,l,b)_{\rm Gal}] dr}{\int_{r_{\rm min}}^{r_{\rm max}} r^2 \rho(R(r,l,b), Z(r,l,b)) dr}.$$

Thus, the total proper motion of each object in the sky is $\boldsymbol{\mu}_{{\rm Sky},i} = \boldsymbol{\mu}_{{\rm R},i} + \boldsymbol{\mu}_{\rm Field}$. Table 5 lists the calculated proper motion for the field and the Galactic proper motion for an object at the distance of the magnetar for both of the targets.

3.2.4. Peculiar Motion

We are interested in back tracing the proper motion of the magnetar to identify its birth site and estimate the time since it left the birth site. The relevant motion for this measurement is the relative proper motion between the magnetar and its progenitor. A reasonable assumption is that the progenitor, likely a young massive star, was moving with the Galactic rotation curve. We define the peculiar motion of the magnetar as the difference between its total proper motion $\boldsymbol{\mu}_{{\rm Sky},i}$ and its expected Galactic proper motion $\boldsymbol{\mu}_{\rm Gal}$, i.e., $\boldsymbol{\mu}_{{\rm Sky},i} = \boldsymbol{\mu}_{\rm Gal} + \boldsymbol{\mu}_{\rm Pec}$.

With this definition, the transverse velocity of the magnetar relative to its neighborhood becomes $r|\boldsymbol{\mu}_{\rm Pec}|$ in a direction θ, s.t. $\tan(\theta) = (\mu_\alpha/\mu_\delta)_{\rm Pec}$ east of north.

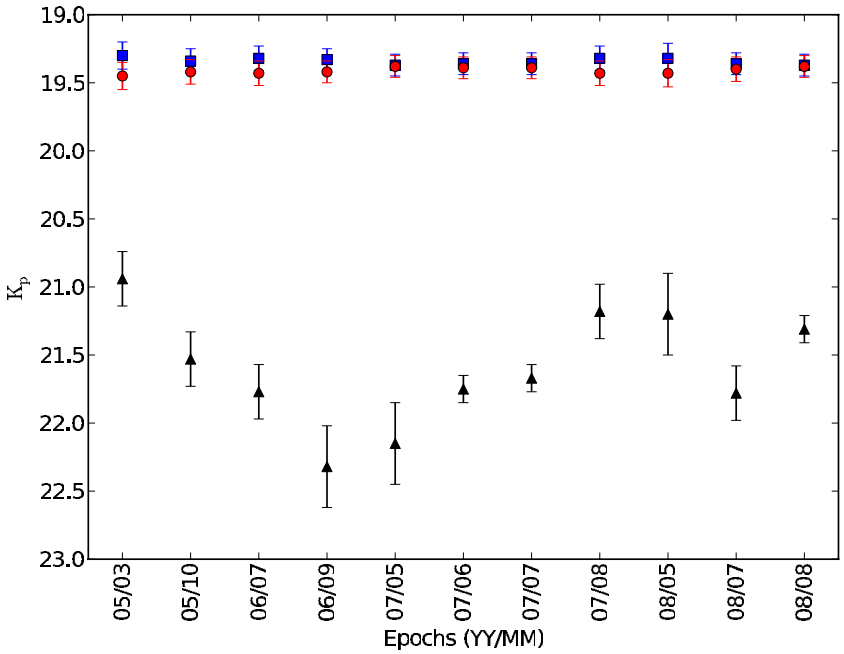

Figure 3. K_p magnitudes of stars around SGR 1806−20 measured over period of 3 years. The circles (red in the online version) correspond to star B and squares (blue in the online version) correspond to star C. The counterpart (star A) of SGR 1806−20 is marked by black triangles. We note a clear variation over a factor of three in the brightness of star A.

(A color version of this figure is available in the online journal.)

3.2.5. Photometry

`StarFinder` calculates flux estimates for stars in the field by scaling the normalized PSF model to best fit the image. We calculate the photometric zero point (ZP) for each image by comparing the magnitudes of stars to the 2MASS Point Source Catalog (Skrutskie et al. 2006) and to published high-resolution studies of the fields that were anchored to the 2MASS catalog. The details of comparison stars for each field are given in Section 4.

4. RESULTS

4.1. SGR 1806−20

We performed PSF fitting on the NIRC2 narrow camera images to identify 71 stars through 10 epochs. The positions of these 71 stars were used for relative astrometry.

We performed relative photometry on the stars A, B, and C in Figure 1. The photometric ZPs were measured by matching the magnitudes of stars B and C to the values measured by Kosugi et al. (2005). Figure 3 shows the measured magnitudes of the three stars. We observe a clear factor of three variation in the brightness of the IR counterpart of SGR 1806−20, star A, thus securing the identification of the IR counterpart of SGR 1806−20.

4.1.1. Proper Motion

Figure 4 shows the measured proper motions of the stars in the SGR 1806−20 field. The field velocity correction was calculated to be $(\mu_\alpha, \mu_\delta)_{\rm Field} = (3.0, 4.8)$ mas yr^{-1}. The proper motion of SGR 1806−20 away from a putative progenitor in the galactic flow is $(\mu_\alpha, \mu_\delta) = (-4.5 \pm 1.4, -6.9 \pm 2.0)$ mas yr^{-1}. Assuming a distance of 9 ± 2 kpc, this corresponds to a linear velocity of 350 ± 100 km s^{-1} with an angle of $213^\circ \pm 10^\circ$ east of north.

Figure 5 shows the direction of motion of SGR 1806−20 with respect to its neighbors. Backtracing this space velocity would put the magnetar close to the cluster of massive stars about 650 years ago.

4.1.2. Other High Proper-motion Stars

In Figure 4, we mark the high proper-motion objects with diamonds and squares. These stars deviate significantly from the dashed green line marking the locus of objects with $\mu_b = 0$, i.e., with zero proper motion along the galactic latitude. These are probably halo stars moving at a high speed through the Galactic disk.

4.2. SGR 1900+14

We observed SGR 1900+14 at 13 epochs with an exposure time of about 1 hr at each observation. Using K_p-band photometry and $H - K_p$ band color (at a single epoch), we present variability and color measurements of SGR 1900+14 and its surrounding stars. Our absolute astrometry is matched to positions as reported by Testa et al. (2008) with an accuracy of 6 mas. They reported a 3σ astrometric uncertainty of $0\farcs81$, which we adopt for comparison with the radio position for Figure 2.

In three images of the SGR 1900+14 field that had excellent AO correction, we detected a faint source (labeled 10 in Figure 2) $0\farcs2$ away from star 3. Source 10 is not detected by Testa et al. (2008) as it was blended with star 3. However, we detected no variation in the combined brightness of stars 3 and 10 in our data and the measurements from Testa et al. (2008) within 0.07 mag. Star 10 is a factor of ∼40 fainter than star 3. With this ratio, assuming no variation in the light from star 3, we can constrain the maximum variation in the brightness of star 10 to be 0.4 mag as compared with the 0.48 mag variation measured for star 7 and no variation for star 3 reported by Testa et al. (2008). Thus, we continue to accept star 7 as the IR counterpart of SGR 1900+14.

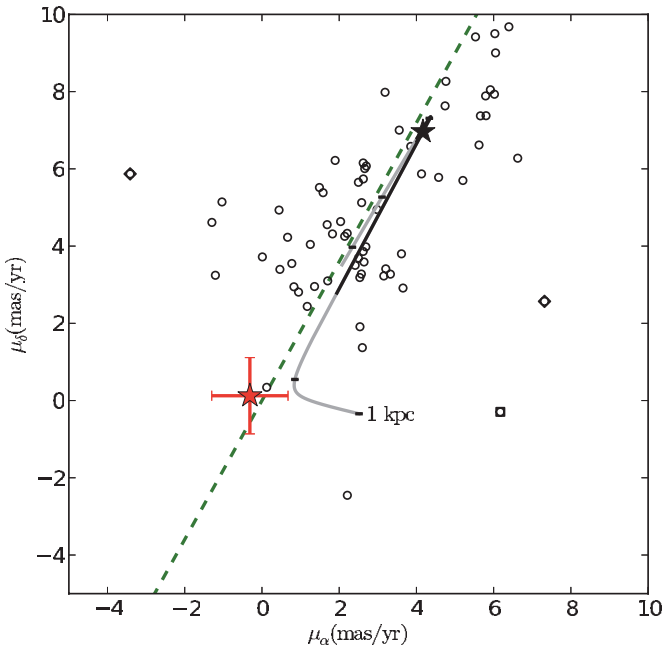

Figure 4. Proper motion of 71 stars in the field of SGR 1806−20 in the sky frame of reference. SGR 1806−20 is marked by the star with error bars (colored red in the online version). The remaining stars have only their best-fit values (hollow black circles) after adding the bulk motion of the field ($\boldsymbol{\mu}_{\rm Field}$ = (3.0, 4.8) mas yr^{-1}; marked by a black "+"). The thick gray line represents the expected motion of stars from 1 to 22.8 kpc along this line of sight, as per the Galactic rotation model presented in Section 3.2.3. Black dashes along the line denote positions 1, 5, 10, 15, and 20 kpc away from the Sun. The section of the line representing objects at a distance of 9 ± 2 kpc from the Sun is marked with a black star and black line to denote the possible motion of the progenitor of SGR 1806−20. The dashed diagonal line (green in the online version) is the locus of objects with $\mu_b = 0$, i.e., with zero proper motion along galactic latitude. Other high proper-motion objects, probably halo stars, are marked by diamonds. The square marks the nominally high proper-motion object near the edge of the detector. However, this measurement may be corrupted by distortion residuals and hence is not considered any further.

(A color version of this figure is available in the online journal.)

4.2.1. Variability

Figure 6 shows the photometry of stars 2–7 (except 5).[4] The median magnitude offsets of stars 2, 3, and 4 were used as relative ZP offsets and the absolute ZP offsets were calculated using K_p magnitudes as reported by Testa et al. (2008). The counterpart suggested by Testa et al. (2008), star 7, was not detected at the edge of star 3 on epochs when the images were not sufficiently deep or the AO performance was not satisfactory. The non-detections were marked with the upper limit on the flux (black triangles). Including the upper limits on flux, star 7 shows slight variability but it is not conclusive.

During our entire observation period from 2005 to 2010, the X-ray counterpart of SGR 1900+14 showed burst activity in only one period from 2006 March to June (Israel et al. 2008). Unfortunately, we have no IR observations between 2005 September and 2006 July. Of these, the AO performance in 2006 July was not satisfactory leading to poor photometry and source confusion. As shown in Table 6, the persistent X-ray luminosity as measured by Israel et al. (2008) and Mereghetti et al. (2006) showed a slight increase in 2006 March and decreased to the pre-burst value by 2006 April. Thus, the lack of NIR variability is not surprising.

[4] Star 5 is excepted from all further discussion since it is far away from the X-ray position error circle and does not affect any of the conclusions. Its identification in the middle of the numbering range is an unfortunate quirk of the numbering scheme that was implemented in previous literature.

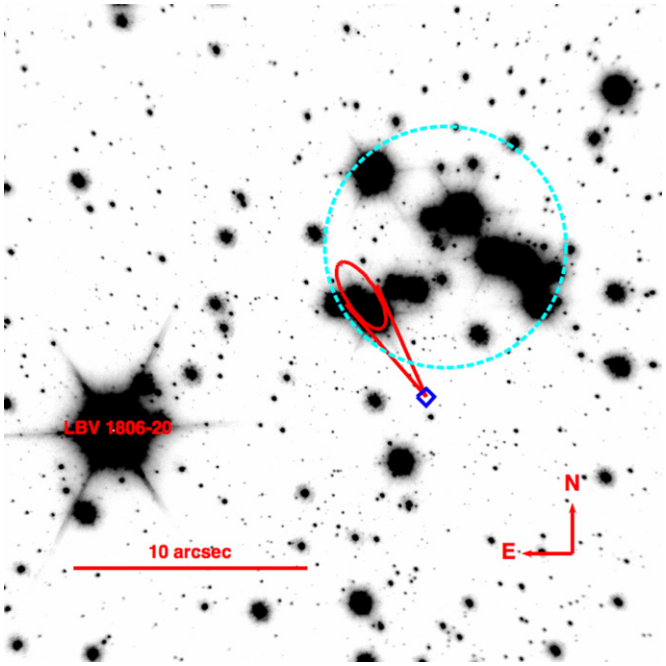

Figure 5. Position of SGR 1806−20 (diamond, blue in the online version) traced back by 0.65 kyr is marked by the ellipse (colored red in the online version). The size of the ellipse denotes the positional uncertainty corresponding to the uncertainty in the proper motion measurement. The solid lines (red in the online version) represent the 1σ limits on the angle of motion. The dashed circle (cyan in the online version) denotes the cluster of massive stars corresponding to the mid-IR source of Fuchs et al. (1999). The position of the luminous blue variable LBV 1806−20 is marked.

(A color version of this figure is available in the online journal.)

Table 6
Persistent X-Ray Luminosity of SGR 1900+14 in the 1–10 keV Band as Reported by Mereghetti et al. (2006) and Israel et al. (2008)

Interval (UTC Date)	F_X (10^{-12} erg cm^{-2} s^{-1})
2005 Sep 20–2005 Sep 22	4.8 ± 0.2^{a}
2006 Mar 25– 2006 Mar 27	4.6 ± 0.8^{b}
2006 Mar 28–2006 Mar 28	6.3 ± 1.7^{b}
2006 Apr 1–2006 Apr 1	5.5 ± 0.4^{a}
2006 Apr 8–2006 Apr 10	5.0 ± 1.4^{b}
2006 Apr 11–2006 Apr 15	5.0 ± 0.7^{b}

Notes.
[a] Absorbed 0.8–12 keV flux from Mereghetti et al. (2006).
[b] Unabsorbed 1–10 keV flux from Israel et al. (2008).

4.2.2. Color Measurement

During the 2007 June 11 observations, we obtained K_p- and H-band images of the field. These images were used to determine the colors of stars near SGR 1900+14. No high-resolution H-band photometry of this field has been performed previously, so we chose to use 2MASS measurements of bright stars to calculate the ZP offsets for the H-band image. The problem with this implementation was that stars bright enough to be included in the 2MASS catalog were saturated in the NIRC2 images that were intended to image the faint magnetar. We rely on the reconstruction of the saturated cores of bright stars by `StarFinder`. This increases the error in photometric measurement and hence in the ZP estimate. We estimate this

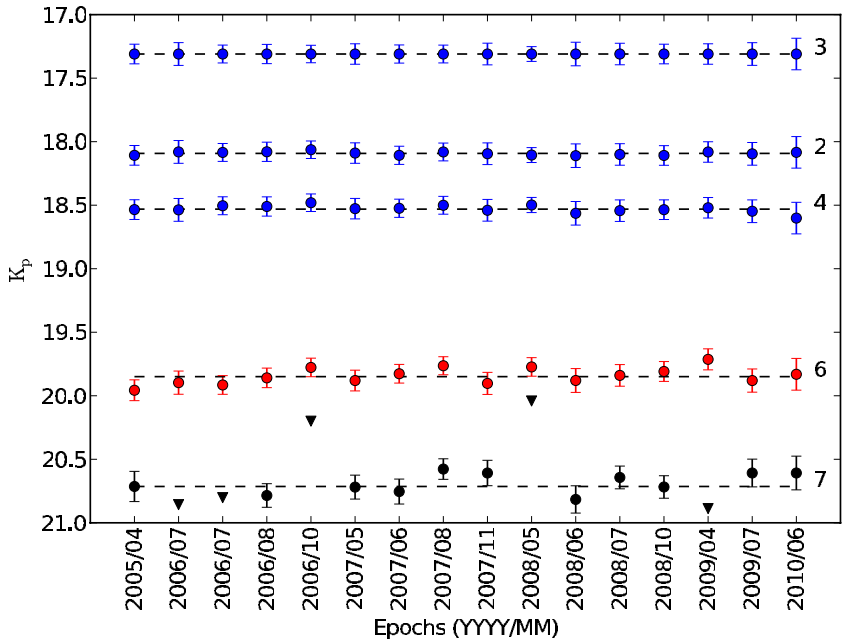

Figure 6. Relative photometry light curves of stars 2–7 (except 5) around SGR 1900+14. To reduce the effect of PSF variations over the field, relative photometry was performed on nearby stars and the absolute calibration was performed by matching stars 2, 3, and 4 to their magnitudes as measured by Testa et al. (2008). The inverted triangles mark 3σ upper limits for star 7 when it was not detected at the edge of star 3.

(A color version of this figure is available in the online journal.)

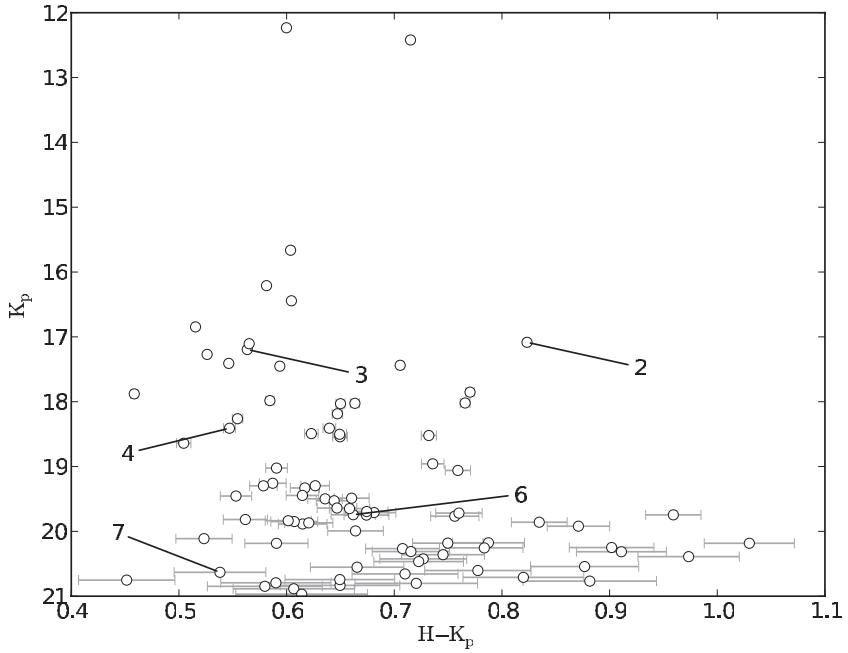

Figure 7. $H - K_p$ color vs. K_p magnitude diagram for 50 stars in the SGR 1900+14 field. Stars 2–7 (except 5) are marked. The H-band image zero point has a systematic uncertainty of ∼0.5 mag, which would effectively only change the scale of the $x-$axis.

systematic error in the H-band ZP to be 0.5 mag. This systematic error changes the scaling on the x-axis of the color–magnitude diagram (Figure 7) and should not change the conclusion if the magnetar were to have a color distinctly different from other stars in the field.

Figure 7 shows an $H - K_p$ color versus K_p magnitude diagram for the 50 stars in the field. Stars 2–7 are labeled. Neither star 6 nor star 7 have abnormal colors and neither is distinctive. There is no clear structure (for example, a main sequence) in the color–magnitude diagram. This is probably due to the varied distances, ages, and extinctions to the stars in this direction. Table 7 lists the H- and K_p-band magnitudes of stars 2–7 (except 5) as shown in Figure 7. Magnetars are not known to fall in a specific color band and our lack of understanding of the background physics prevents us from predicting the shape of the IR emission spectrum (Testa et al. 2008). We conclude that the lack of a distinctive color for any star near the location of SGR 1900+14 is not significant.

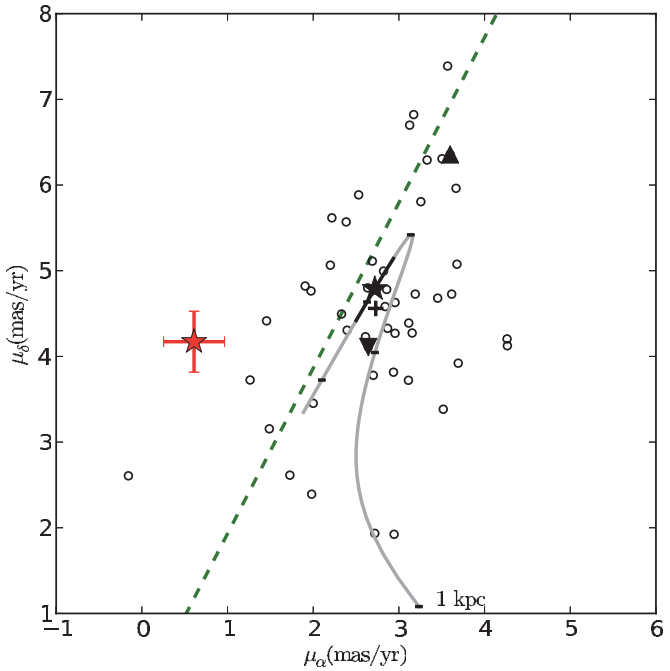

Figure 8. Proper motion of 50 stars in the field of SGR 1900+14 in the sky frame of reference. The putative counterpart of SGR 1900+14 is marked by the star with error bars (colored red in the online version). The proper motions of star 6 (solid black triangle) and star 3 (inverted black triangle) seem to lie along the Galactic rotation curve. The remaining stars have only their best-fit values (hollow black circles) after adding the bulk motion of the field ($\boldsymbol{\mu}_{\rm Field} = (2.7, 4.6)$ mas yr^{-1}) (marked by a black +). The thick gray line represents the expected motion of stars from 1 to 19.8 kpc along this line of sight, as per the Galactic rotation model presented in Section 3.2.3. Black dashes along the line denote positions 1, 5, 10, 15, and 20 kpc away from the Sun. The section of the line representing objects at a distance of 12.5 ± 1.7 kpc from the Sun is marked with a black star and a black line to denote the possible motion of the progenitor of SGR 1900+14. The dashed diagonal line (green in the online version) is the locus of objects with $\mu_b = 0$, i.e., with zero proper motion along galactic latitude.

(A color version of this figure is available in the online journal.)

Table 7
H- and K_p-band Photometry for Stars 2–7 (Except 5) Near SGR 1900+14

Object ID	R.A. (J2000) (deg)	Decl. (J2000) (deg)	H Band (mag)	K_p Band (mag)
2	$19^{\rm h}07^{\rm d}14\overset{\rm s}{.}28$	$9°19'18\overset{''}{.}84$	18.57 ± 0.003	17.98 ± 0.002
3	$19^{\rm h}07^{\rm d}14\overset{\rm s}{.}30$	$9°19'19\overset{''}{.}63$	17.76 ± 0.002	17.19 ± 0.001
4	$19^{\rm h}07^{\rm d}14\overset{\rm s}{.}28$	$9°19'19\overset{''}{.}78$	18.96 ± 0.005	18.41 ± 0.003
6	$19^{\rm h}07^{\rm d}14\overset{\rm s}{.}34$	$9°19'19\overset{''}{.}92$	20.41 ± 0.02	19.74 ± 0.01
7	$19^{\rm h}07^{\rm d}14\overset{\rm s}{.}31$	$9°19'19\overset{''}{.}74$	21.17 ± 0.04	20.63 ± 0.02

Note. The zero-point error in the photometry is 0.5 mag for H band and 0.1 mag for K_p band.

4.2.3. Proper Motion

Figure 8 shows the measured proper motions of 50 stars in the neighborhood of SGR 1900+14. The velocity offset, calculated from the galactic rotation, is $(\mu_\alpha, \mu_\delta)_{\rm Field} = (2.7, 4.6)$ mas yr^{-1}. For star 7, we calculate a proper motion of $(\mu_\alpha, \mu_\delta) = (-2.1 \pm 0.4, 0.6 \pm 0.5)$ mas yr^{-1} away from a putative progenitor moving with the galactic flow. At a distance of 12.5 ± 1.7 kpc, this corresponds to a transverse space velocity of 130 ± 30 km s^{-1}.

Figure 9 shows the direction of motion of SGR 1900+14 with respect to its neighbors. Backtracing this space velocity would put the magnetar close to the cluster of massive stars about 6 kyr ago.

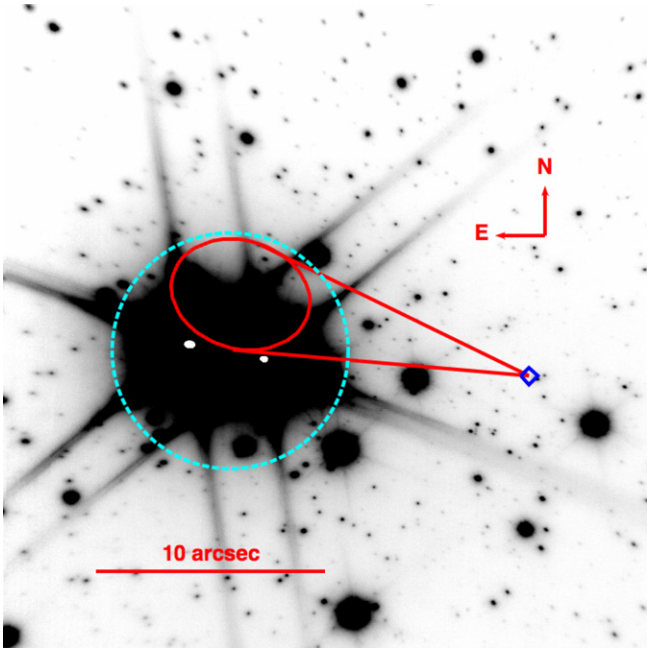

Figure 9. Position of the putative counterpart of SGR 1900+14 (blue diamond) traced back by 6 kyr is marked by the solid ellipse (red in the online version). The size of the ellipse denotes the positional uncertainty corresponding to the uncertainty in the proper motion measurement. The solid (red) lines represent the 1σ limits on the angle of motion. The dashed circle (cyan in the online version) denotes the cluster of massive stars (Vrba et al. 2000).

(A color version of this figure is available in the online journal.)

Table 8
Proper Motions Measured for Stars 2–7 Near SGR 1900+14

Object	$\boldsymbol{\mu}_{\rm Pec}$ (mas yr^{-1})	Velocity (km s^{-1})	Direction E of N
2	$(-0.11, -0.55)$	33 ± 25	191 ± 143
3	$(-0.08, -0.67)$	40 ± 25	...
4	$(-0.74, -2.39)$	148 ± 30	197 ± 10
6	$(+0.88, +1.58)$	107 ± 30	30 ± 12
7	$(-2.11, -0.61)$	130 ± 30	254 ± 10

Notes. The values have been corrected for the galactic rotation offsets. The transverse space velocities are calculated assuming a distance of 12.5 kpc. 1σ error bars on $\boldsymbol{\mu}_{\rm Pec}$ are (0.4, 0.5) mas yr^{-1}.

Star 6 and star 3 are the only two other sources detected inside the 3σ error circle around the radio position of SGR 1900+14. Their velocities are marked by a black triangle (Star 6) and an inverted black triangle (Star 3) in Figure 8. Their velocities suggest that these are regular galactic stars moving in the plane of the galaxy (dashed green line).

Table 8 gives the proper motions measured for each of the stars 2–7 along with their corresponding transverse space velocity assuming a distance of 12.5 kpc.

5. DISCUSSION

Using LGS-AO supported near-IR observations, we have measured the proper motions of SGR 1806−20 and SGR 1900+14 to be $(\mu_\alpha, \mu_\delta) = (-4.5, -6.9) \pm (1.4, 2.0)$ mas yr^{-1} and $(\mu_\alpha, \mu_\delta) = (-2.1, -0.6) \pm (0.4, 0.5)$ mas yr^{-1}, respectively. These correspond to a linear transverse velocity of 350 ± 100 km s^{-1} and 130 ± 30 km s^{-1}, respectively, at the measured distances of their putative associations. Previously, using very long baseline

interferometry (VLBI) at radio wavelengths, transverse linear velocities have been measured only for two magnetars: AXP 1E 1810−197: $212 \pm 35\,\mathrm{km\,s^{-1}}$ (Helfand et al. 2007) and AXP PSR J1550−5418: $280 \pm 120\,\mathrm{km\,s^{-1}}$ (Deller et al. 2012). The radio counterpart for AXP PSR J1622−4950 has been recently identified by Levin et al. (2010) and would lead to an accurate proper motion measurement with VLBI. With the transverse velocity measurements for two AXPs and two SGRs in the 100–400 $\mathrm{km\,s^{-1}}$ range, it is highly unlikely that each of these objects has an extremely high radial velocity component. Hence, we conclude that magnetars as a family do not possess the high space velocities ($\sim$1000 $\mathrm{km\,s^{-1}}$) that were expected earlier (cf. Rothschild & Lingenfelter 1996).

Consider the space velocities of other families of neutron stars in contrast with magnetars. Canonical radio pulsars ($B \sim 10^{11}$ G) have typical space velocities of $\sim$200–300 $\mathrm{km\,s^{-1}}$ (Hobbs et al. 2005). Tetzlaff et al. (2010) traced the motions of four young, hot X-ray bright isolated neutron stars to associate them with progenitors and constrain their ages. They calculated the space velocities of these objects to be $\sim 350 \pm 180\,\mathrm{km\,s^{-1}}$. There are a few fast moving pulsars such as PSR J1357−6429, which is a Vela-like radio pulsar with a transverse velocity of 1600–2000 $\mathrm{km\,s^{-1}}$ (Kirichenko et al. 2012), but these seem to be outliers from the family.

From these data, we observe that perhaps velocities are not a good discriminator of different groups of neutron stars and their origins.

5.1. Association

Our measured proper motions provide very good evidence linking SGR 1806−20 to the cluster of massive stars. The time required for SGR 1806−20 to move from the cluster to its current position is 650 ± 300 yr. It may not be a surprise that one of the younger supernovae in our galaxy resulted from the magnetar. However, SGR 1806−20 lies in the galactic plane behind dust clouds, which create very high extinction in the visible wavelengths. Hence, the supernova associated with the magnetar may not have been visible to the naked eye. For SGR 1900+14, we rule out any association with the SNR G 42.8+0.6 and confirm that this magnetar is associated with the star cluster. The time to trace the magnetar back to the cluster is 6 ± 1.8 kyr.

The turn-off masses for the clusters with which the magnetars are associated allow us to place lower limits on the progenitor masses of these magnetars. Currently, progenitor mass estimates exist for three of the magnetars:

SGR 1806−20: $48^{+20}_{-8}\,M_\odot$ (Bibby et al. 2008),

CXO J1647−455: $>40\,M_\odot$ (Muno et al. 2006; Ritchie et al. 2010), and

SGR 1900+14: $17 \pm 2\,M_\odot$ (Davies et al. 2009).

We note that only the two youngest SGRs have a star cluster in their vicinity. The lack of a star cluster in the vicinity of the older SGRs (despite ages of 4–10 kyr) suggests that it is not essential that SGRs should be associated with star clusters. Furthermore, the inferred progenitor masses of SGR 1900+14 does not compel us to believe that SGRs arise from massive stars. We conclude that binarity likely has a bigger role in forming SGRs.

5.2. Braking Index

If the association of the SGRs with the star clusters is taken for granted, we can constrain the braking index of the magnetars. The braking index n is calculated from the following implicit equation:

$$n = 1 + \frac{P}{T\dot{P}}(1 - (P_0/P)^{(n-1)}).$$

Here, T is the kinematic age of the magnetar (time taken to move from cluster to present position) and P_0 is the spin period at birth.

The instantaneous $\dot{P}$ is known to vary by a factor of three to four corresponding to large variations of braking torque on the magnetar (Woods et al. 2002, 2007). We use the X-ray timing measurements from Kouveliotou et al. (1998), Mereghetti et al. (2005b), Woods et al. (2007), Marsden et al. (1999), Woods et al. (2002), Woods et al. (2003), Mereghetti et al. (2006), and Nakagawa et al. (2009) to calculate an average $\dot{P}$ of $49 \times 10^{-11}\,\mathrm{s\,s^{-1}}$ for SGR 1806−20 and $17 \times 10^{-11}\,\mathrm{s\,s^{-1}}$ for SGR 1900+14 from 1996 to 2006.

Assuming $P_0/P \ll 1$, we estimate n to be $1.76^{+0.65}_{-0.24}$ for SGR 1806−20 and $1.16^{+0.04}_{-0.07}$ for SGR 1900+14. This is significantly smaller than the canonical value of $n = 3$ for the magnetic dipole spin-down mechanism for pulsars. Low braking indices have been discussed in the context of twisted magnetospheres (e.g., Thompson et al. 2002) and particle wind spin-down (e.g., Tong et al. 2012). However, the large variations in $\dot{P}$ over tens of years imply that these measurements cannot be taken at face value.

We thank M. van Kerkwijk and C. Thompson for their critical comments and extensive discussions. The data presented herein were obtained at the W. M. Keck Observatory, which is operated as a scientific partnership among the California Institute of Technology, the University of California and the National Aeronautics and Space Administration. The Observatory was made possible by the generous financial support of the W. M. Keck Foundation.

Facilities: Keck:II(NIRC2, LGS AO)

REFERENCES

Bertin, E., & Arnouts, S. 1996, A&AS, 117, 393
Bibby, J. L., Crowther, P. A., Furness, J. P., & Clark, J. S. 2008, MNRAS, 386, L23
Binney, J., & Tremaine, S. 2008, Galactic Dynamics (2nd ed.; Princeton, NJ: Princeton Univ. Press)
Cameron, P. B., Britton, M. C., & Kulkarni, S. R. 2009, AJ, 137, 83
Cameron, P. B., Chandra, P., Ray, A., et al. 2005, Nature, 434, 1112
Davies, B., Figer, D. F., Kudritzki, R.-P., et al. 2009, ApJ, 707, 844
de Luca, A., Caraveo, P. A., Esposito, P., & Hurley, K. 2009, ApJ, 692, 158
Dehnen, W., & Binney, J. J. 1998, MNRAS, 298, 387
Deller, A. T., Camilo, F., Reynolds, J. E., & Halpern, J. P. 2012, ApJ, 748, L1
Diolaiti, E., Bendinelli, O., Bonaccini, D., et al. 2000, Proc. SPIE, 4007, 879
Eikenberry, S. S., Matthews, K., LaVine, J. L., et al. 2004, ApJ, 616, 506
Eisenhauer, F., Schödel, R., Genzel, R., et al. 2003, ApJ, 597, L121
Figer, D. F., Najarro, F., & Kudritzki, R. P. 2004, ApJ, 610, L109
Frail, D. A., Kulkarni, S. R., & Bloom, J. S. 1999, Nature, 398, 127
Fuchs, Y., Mirabel, F., Chaty, S., et al. 1999, A&A, 350, 891
Gaensler, B. M., Kouveliotou, C., Gelfand, J. D., et al. 2005, Nature, 434, 1104
Hartmann, D., Vrba, F., Luginbuhl, C., et al. 1996, in AIP Conf. Ser. 366, High Velocity Neutron Stars, ed. R. E. Rothschild & R. E. Lingenfelter (Melville, NY: AIP), 84
Helfand, D. J., Chatterjee, S., Brisken, W. F., et al. 2007, ApJ, 662, 1198
Hobbs, G., Lorimer, D. R., Lyne, A. G., & Kramer, M. 2005, MNRAS, 360, 974
Hurley, K. 2011, Phys. E, 43, 681
Hurley, K., Boggs, S. E., Smith, D. M., et al. 2005, Nature, 434, 1098
Hurley, K., Cline, T., Mazets, E., et al. 1999, Nature, 397, 41
Israel, G., Covino, S., Mignani, R., et al. 2005, A&A, 438, L1
Israel, G. L., Romano, P., Mangano, V., et al. 2008, ApJ, 685, 1114
Jurić, M., Ivezić, Ž., Brooks, A., et al. 2008, ApJ, 673, 864

Kaplan, D. L., Chatterjee, S., Hales, C. A., Gaensler, B. M., & Slane, P. O. 2009, AJ, 137, 354
Kaplan, D. L., Fox, D. W., Kulkarni, S. R., et al. 2002, ApJ, 564, 935
Kirichenko, A., Danilenko, A., Mennickent, R. E., et al. 2012, in ASP Conf. Proc., Electromagnet Radiation from Pulsars and Magnetars, ed. W. Lewandowski (San Francisco, CA: ASP), in press (arXiv:1206.5149)
Kosugi, G., Ogasawara, R., & Terada, H. 2005, ApJ, 623, L125
Kouveliotou, C., Dieters, S., Strohmayer, T., et al. 1998, Nature, 393, 235
Kouveliotou, C., Fishman, G. J., Meegan, C. A., et al. 1993, Nature, 362, 728
Kouveliotou, C., Strohmayer, T., Hurley, K., et al. 1999, ApJ, 510, L115
Kulkarni, S. R., Matthews, K., Neugebauer, G., et al. 1995, ApJ, 440, L61
Laros, J. G., Fenimore, E. E., Fikani, M. M., Klebesadel, R. W., & Barat, C. 1986, Nature, 322, 152
Levin, L., Bailes, M., Bates, S., et al. 2010, ApJ, 721, L33
Marsden, D., Rothschild, R. E., & Lingenfelter, R. E. 1999, ApJ, 520, L107
Mazets, E. P., Golenetskij, S. V., & Guryan, Y. A. 1979, Sov. Astron. Lett., 5, 343
McClure-Griffiths, N. M., & Gaensler, B. M. 2005, ApJ, 630, L161
Mereghetti, S. 2008, A&AR, 15, 225
Mereghetti, S., Esposito, P., Tiengo, A., et al. 2006, ApJ, 653, 1423
Mereghetti, S., Götz, D., von Kienlin, A., et al. 2005a, ApJ, 624, L105
Mereghetti, S., Tiengo, A., Esposito, P., et al. 2005b, ApJ, 628, 938
Muno, M. P., Clark, J. S., Crowther, P. A., et al. 2006, ApJ, 636, L41
Nakagawa, Y. E., Mihara, T., Yoshida, A., et al. 2009, PASJ, 61, 387
Palmer, D. M., Barthelmy, S., Gehrels, N., et al. 2005, Nature, 434, 1107
Ritchie, B. W., Clark, J. S., Negueruela, I., & Langer, N. 2010, A&A, 520, A48
Rothschild, R. E., & Lingenfelter, R. E. (ed.) 1996, AIP Conf. Ser. 366, High Velocity Neutron Stars (Melville, NY: AIP)
Skrutskie, M. F., Cutri, R. M., Stiening, R., et al. 2006, AJ, 131, 1163
Spreeuw, H., Scheers, B., & Wijers, R. A. M. J. 2010, A&A, 509, A99
Svirski, G., Nakar, E., & Ofek, E. O. 2011, MNRAS, 415, 2485
Testa, V., Rea, N., Mignani, R. P., et al. 2008, A&A, 482, 607
Tetzlaff, N., Neuhäuser, R., Hohle, M. M., & Maciejewski, G. 2010, MNRAS, 402, 2369
Thompson, C., & Duncan, R. C. 1993, ApJ, 408, 194
Thompson, C., & Duncan, R. C. 1995, MNRAS, 275, 255
Thompson, C., & Duncan, R. C. 1996, ApJ, 473, 322
Thompson, C., Lyutikov, M., & Kulkarni, S. R. 2002, ApJ, 574, 332
Tong, H., Xu, R. X., Song, L. M., & Qiao, G. J. 2012, arXiv:1205.1626
van Dam, M. A., Bouchez, A. H., Le Mignant, D., et al. 2006, PASP, 118, 310
van Kerkwijk, M. H., Kulkarni, S. R., Matthews, K., & Neugebauer, G. 1995, ApJ, 444, L33
Vasisht, G., Kulkarni, S. R., Frail, D. A., & Greiner, J. 1994, ApJ, 431, L35
Vink, J., & Kuiper, L. 2006, MNRAS, 370, L14
Vrba, F. J., Henden, A. A., Luginbuhl, C. B., et al. 2000, ApJ, 533, L17
Vrba, F. J., Luginbuhl, C. B., Hurley, K. C., et al. 1996, ApJ, 468, 225
Wachter, S., Ramirez-Ruiz, E., Dwarkadas, V. V., et al. 2008, Nature, 453, 626
Wizinowich, P. L., Le Mignant, D., Bouchez, A. H., et al. 2006, PASP, 118, 297
Woods, P. M., Kouveliotou, C., Finger, M. H., et al. 2007, ApJ, 654, 470
Woods, P. M., Kouveliotou, C., Göğüş, E., et al. 2002, ApJ, 576, 381
Woods, P. M., Kouveliotou, C., Göğüş, E., et al. 2003, ApJ, 596, 464